Journal of Geophysical Research: Atmospheres

RESEARCH ARTICLE
10.1029/2017JD028068

Microphysical Properties of Tropical Tropopause Layer Cirrus

Sarah Woods[1], R. Paul Lawson[1], Eric Jensen[2], T. P. Bui[2], Troy Thornberry[3], Andrew Rollins[3], Leonhard Pfister[2], and Melody Avery[4]

[1]SPEC, Inc., Boulder, CO, USA, [2]NASA Ames Research Center, Moffet Field, CA, USA, [3]NOAA ESRL/CIRES, Boulder, CO, USA, [4]NASA Langley Research Center, Hampton, VA, USA

Key Points:
- Ice particles were predominantly quasi-spheroidal, especially at coldest temperatures
- Growth-sedimentation is dominant in determining TTL cirrus size distributions and habits
- Aggregation is negligible in TTL in situ cirrus

Correspondence to:
S. Woods,
swoods@specinc.com

Citation:
Woods, S., Lawson, R. P., Jensen, E., Bui, T. P., Thornberry, T., Rollins, A., et al. (2018). Microphysical properties of tropical tropopause layer cirrus. *Journal of Geophysical Research: Atmospheres*, *123*, 6053–6069. https://doi.org/10.1029/2017JD028068

Received 15 DEC 2017
Accepted 23 APR 2018
Accepted article online 4 MAY 2018
Published online 4 JUN 2018

Abstract Pervasive cirrus clouds in the tropical tropopause layer (TTL) play an important role in determining the composition of stratospheric air through dehydration of tropospheric air entering the stratosphere. This dehydration affects Earth's energy budget and climate, yet uncertainties remain regarding the microphysical processes that govern TTL cirrus. TTL cirrus were sampled with the NASA Global Hawk UAV for over 30 hr in the Western Pacific in 2014 during the Airborne Tropical TRopopause EXperiment. In situ measurements by a Fast Cloud Droplet Probe and Hawkeye probe (combination Fast Cloud Droplet Probe, Two-Dimensional Stereo optical array probe, and Cloud Particle Imager) provided particle concentrations and sizing between 1- and 1,280-μm diameter and high resolution images for habit identification. We present the variability in ice concentrations, size distributions, and habits as functions of temperature, altitude, and time since convective influence. Observed ice particles were predominantly small and quasi-spheroidal in shape, with the percentage of quasi-spheroids increasing with decreasing temperature. In comparison to the large fraction of the population consisting of quasi-spheroids, faceted habits (columns, plates, rosettes, and budding rosettes) constituted a smaller percentage of the overall population and exhibited the opposite correlation with temperature. The trend of higher percentages of faceted crystals occurring at warmer temperatures may be due to diffusional growth or aggregation as particles descend through cloud, and/or the more rapid diffusional growth rate at warmer temperatures. Sampling was typically well away from deep convection, however, and very few aggregates were observed, so the trend of higher percentages of faceted habits is likely attributable to diffusional growth.

1. Introduction

The tropical tropopause layer (TTL, ~13–18 km) largely controls the composition of the stratosphere through physical processes occurring at this transitional layer between the troposphere and stratosphere. Several TTL physical processes affect stratospheric humidity, ozone, and the Earth's radiation budget: deep convective transport of chemical constituents, such as water vapor, into the TTL; the formation of ubiquitous thin cirrus in the TTL, which themselves have a large effect on the radiation budget and climate (Comstock et al., 2002; Forster & Shine, 2002; Haladay & Stephens, 2009; McFarquhar et al., 2000; Ulanowski et al., 2006); effects on stratospheric humidity by sedimenting ice crystals in TTL cirrus (Jensen et al., 2013a; Rollins et al., 2016); slow vertical transport of air masses through the TTL; and the effects of tropical atmospheric waves on TTL thermal structure, dehydration, and transport (Jensen et al., 2016; Kim et al., 2016; Schoeberl et al., 2015; Ueyama et al., 2015), among others. Recent studies suggest that changes in stratospheric humidity may have significant impacts on climate over those associated with decadal increases in greenhouse gases (Riese et al., 2012; Solomon et al., 2010). As such, future concentration variations in stratospheric humidity in response to changing climate are a significant climate feedback, and improving understanding of TTL physical processes are important for constraining future concentrations of stratospheric humidity.

Key in improving understanding of these physical processes is understanding the microphysics that govern the life cycle of TTL cirrus ice particles, which is influenced by such environmental factors as the proximity of convection as a source of already developed ice and moisture, the ambient water vapor field, relative humidity, temperature, and the air mass history. Convection brings up moisture and ice, but larger ice crystals are quickly removed from the TTL by sedimentation. As suggested by the ensuing analysis, the large crystals fall out, and the smaller ice can survive on an hourly time scale. The air mass travels downstream, hits a cold pool, and forms or regrows any surviving crystals in situ via waves, radiatively driven events, moderately small

increases in relative humidity, and so forth. These events affect the cirrus ice concentration, size, and habit, which have been shown to affect the scattering properties of the particles (Mishchenko et al., 1996; Ulanowski et al., 2006). These scattering properties can strongly influence the net radiative forcing of cirrus clouds, which play an important role in the Earth-atmosphere radiation balance (Baran, 2009; Wendisch et al., 2007, and references therein).

The habit of the ice particle depends upon the ambient environmental conditions under which the ice crystal formed and grew. With decreasing temperature, ice usually forms before −28°C, and at −28°C, polycrystals begin forming (Bailey & Hallett, 2009). If an aqueous solution freezes, it freezes in a quasi-spheroid, droxtal, or other forms (Jarvinen et al., 2016). These quasi-spheroids could be interpreted as germ rosettes, from which the ice particle can grow into a budding or bullet rosette with increasing temperature (decreasing altitude) under supersaturated conditions. Bullet rosettes start at −40°C and grow via vapor deposition, often observed hundreds of kilometers downwind of the anvil. In fresh outflow from a thunderstorm anvil, habits are overwhelmingly aggregates. But, a few hours downwind of an anvil, one can observe rosettes due to in situ regrowth of the particles in the anvil outflow that do not sediment out immediately. Airborne Tropical TRopopause EXperiment (ATTREX) sampling was normally well away from convection, and though the moisture providing saturation sufficient for particle growth may have come from convection, the clouds sampled were primarily in situ cirrus.

Compared to observations in other climatically important regions around the globe, observations of TTL composition are sparse. This is due, in part, to the inherent challenges with aircraft sampling of the high TTL altitude. The sparse in situ observations of TTL cirrus that have been collected to date that contain information for ice habit identification include very limited observations from the NASA WB-57F over the Marshall Islands in 1973 (Heymsfield, 1986; McFarquhar et al., 2000), during the Costa Rica-Aura Validation Experiment (CR-AVE) in 2006 (Jensen et al., 2008; Lawson et al., 2008) and from the Tropical Composition, Clouds, and Climate Coupling (TC4) experiment off the Pacific Coast of Central America in 2007 (Davis et al., 2010; Lawson et al., 2010). The observations from the Marshall Islands in 1973 were composed of replicator data collected from a slow 3-min ascent through cloud at −84°C and indicated that particles primarily ranged from 5 to 50 μm in maximum diameter, with habits consisting mostly of columns and trigonal plates as well as some hexagonal plates. The CR-AVE measurements from 2006 included particles of larger size than were observed in the 1973 data, extending to around 160 μm in maximum diameter, although the vast majority of the ice crystals were smaller than 50 μm. These measurements differed in habit observation from that of the 1973 flight, with 84% quasi-spheroids, and particles larger than 65 μm showing characteristics of hexagonal plates. The composition of habits from the Marshall Islands campaign likely varied from those of subsequent campaigns because these replicator observations were limited to a single ascent through cloud, and so are not statistically representative of the cirrus in time or geographic extent, but rather represent a very small subset of the observations of CR-AVE, TC4, and ATTREX. The TC4 measurements were not ideal for habit data because the high-resolution images were limited. Additional in situ measurements have been collected with forward scattering probes, sometimes accompanied by optical array probes (Krämer et al., 2016; Thomas et al., 2002, and references therein), but these observations were limited in that they did not include high-resolution imagery for identification of particle habit. As a result, TTL processes are not well represented in global models. The ATTREX project provided data needed to address these shortcomings: extensive, high spatial resolution measurements over large geographical regions in the Tropical Pacific. This work utilizes this key data set to investigate the variability in ice concentrations, size distributions, and habits as functions of temperature, altitude, and time since convective influence in TTL cirrus.

2. Measurements

The NASA ATTREX collected observations in the TTL over a 5-year science campaign with the NASA Global Hawk UAV (unmanned aerial vehicle). The campaign focused on collecting observations of TTL physical and chemical properties to provide insight on these processes and facilitate improving our understanding of the processes governing water vapor transport to the stratosphere. Here we focus on observations of TTL cirrus microphysical properties, which play an important role in dehydration of tropospheric air as it enters the stratosphere. The 2011, 2013, and 2015 flights were based out of NASA Armstrong Flight Research Center in California; the 2014 flights were conducted out of Guam. Each science flight lasted, on

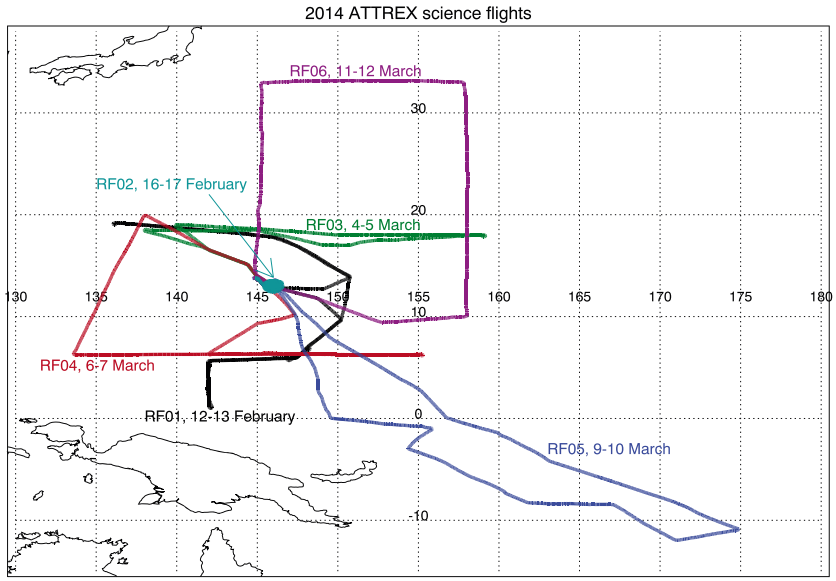

Figure 1. Overlay of all UAV6 science flights from the January–March 2014 deployment out of Guam. ATTREX = Airborne Tropical TRopopause EXperiment.

average, 24 hr for the flights out of California and around 12–19 hr (16.3 hr on average) for the flights out of Guam.

For cloud microphysical observations, the 2011–2013 flights had a Fast Cloud Droplet Probe (FCDP; Lawson et al., 2017), onboard, which provides particle concentration and sizing between 1 and 50 μm. In 2014, a Hawkeye instrument was added to the payload. The Hawkeye combines a FCDP, a two-dimensional stereo optical array probe (2D-S; Lawson, O'Connor, et al., 2006) and a cloud particle imager (CPI; Lawson et al., 2001), yielding measurement of particle concentration and area, and calculation of particle mass size distributions for particles between 1 and 1,280 μm (1–50 μm by the FCDP and 10–1,280 μm by the 2D-S). The CPI also provides high-resolution (2.3-μm pixel) cloud particle images over the size range of 2.3–2,300 μm used for habit identification. Throughout the current work, particle size refers to the maximum length of the particle across its 2-D projected area, as observed by the respective instrument. See below for additional instrument detail. We present analysis from the ATTREX-2014 data set since the addition of the Hawkeye and the prime deployment location in Guam yielded a multitude of high-quality in situ cloud sampling in the Western Pacific during Boreal winter. Figure 1 shows the 2014 science flight paths from Guam, during which TTL sampling was conducted by continuously profiling the aircraft between approximately 45 and 60 kft (13.5

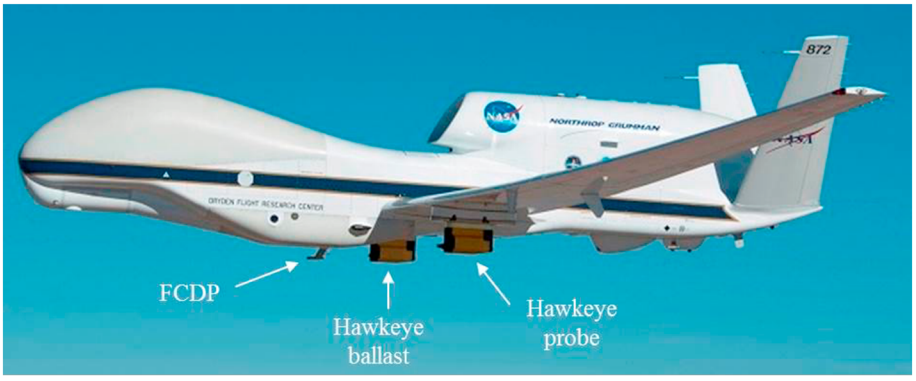

Figure 2. Photo showing installation location of the Fast Cloud Droplet Probe (FCDP), Hawkeye probe, and aerodynamic Hawkeye ballast on Global Hawk UAV6.

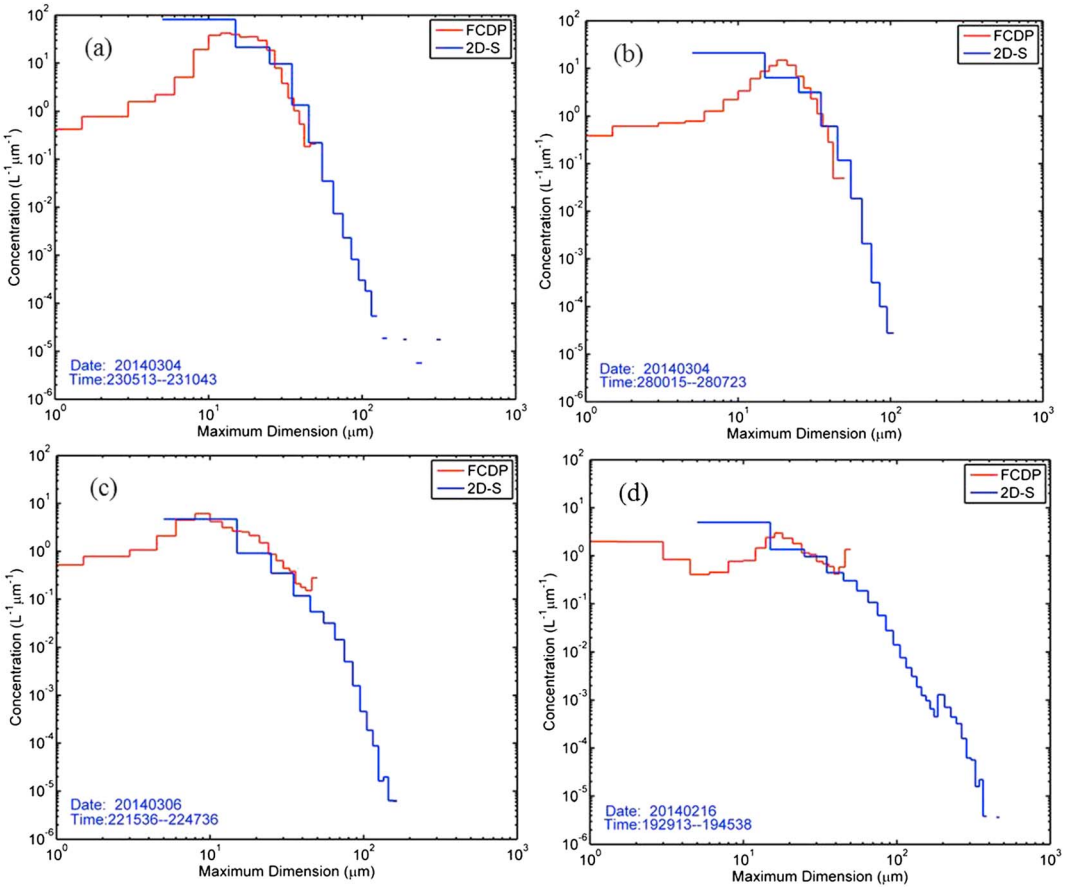

Figure 3. Example Fast Cloud Droplet Probe (FCDP) and Two-Dimensional Stereo optical array probe (2D-S) size distributions showing the agreement between the two instruments over the size range of overlap.

and 18 km), yielding over 34 hr of TTL cirrus sampling. Additional details of the experiment are provided in Jensen et al. (2015) and Jensen et al. (2013b). In terms of sampling, it should be noted that (1) the aircraft did not fly in close proximity to deep convection and (2) the aircraft was often, but not always, prevented from climbing all of the way to cloud top because either (a) the aircraft ceiling was too low given fuel loading or (b) the temperatures at cloud top fell below the Global Hawk safety limit.

Figure 2 shows a photograph of the Global Hawk during ATTREX, indicating the locations of the cloud probes. The FCDP was installed under the fuselage of the aircraft, and the Hawkeye underneath the wing, complemented by a Hawkeye shell on the opposite wing to balance drag on the aircraft. The FCDP and Hawkeye-FCDP utilize forward scattered laser light by each particle that enters the sample volume to provide particle concentration and diameter sizing between 1 and 50 μm, with an approximately 2-μm resolution. From the concentration and sizing, particle area and mass over this size range are estimated assuming spherical ice particles since the exact shape of the particles is not known. For further details of the processing of the FCDP data and estimated uncertainties, see Lawson et al. (2017) and Thornberry et al. (2017). Although some uncertainty in the FCDP sizing exists due to the assumption of spherical particles, the FCDP size distributions show generally good agreement with the 2D-S size distributions in the size region of measurement overlap (between about 10 and 45 μm), as shown by the representative examples plotted in Figure 3 discussed below. The FCDP generally provided higher counting statistics than the Hawkeye-FCDP, so the FCDP data are used for all but two flights. During the flights on 16 February and 11 March, the FCDP did not provide data, so the Hawkeye-FCDP data are used for these two flights.

The Hawkeye-2D-S is same in design as the 2D-S, except that it has a 50-mm-diameter sample tube rather than an open sampling path in order to integrate it with the CPI. Hereafter, it will be referred to as

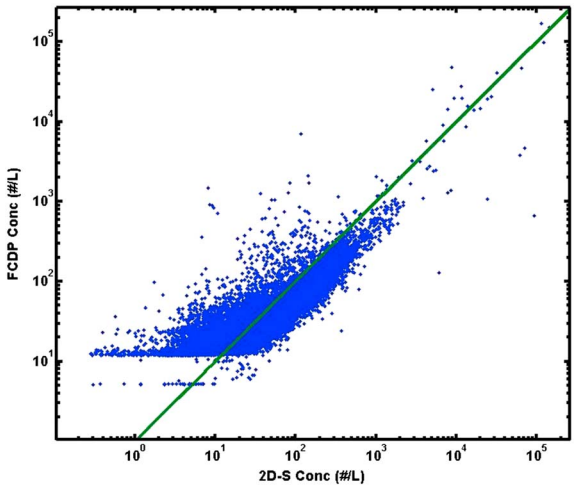

Figure 4. Scatter plot comparing Fast Cloud Droplet Probe (FCDP) and Two-Dimensional Stereo optical array probe (2D-S) 10-s averaged total concentration over the size range of overlap (10–45 μm). The solid line represents a 1:1 ratio.

the 2D-S. The 2D-S is composed of two 128 photo diode arrays that are occulted when a particle passes through the sample volume, thus producing a 2-D projected image of the particle. When both optical arrays report good data, the average of the two channels is reported. If data are missing from one of the two arrays, data from the other channel are used. Due to the generally low concentrations in TTL cirrus, out-of-focus particles are included in the analysis. For sizing the 2D-S images smaller than about 135 μm that are out-of-focus, the reconstruction method described by Korolev (2007) is used, which assumes the particles were originally spherical. The original shape of the particle is actually unknown, but most of the in-focus particles have aspect ratios close to one, so using the Korolev (2007) reconstruction is deemed the best approach for estimating the actual size. For sizes larger than about 135 μm, the maximum length of the particle in any direction of the 2-D image (irrespective of the *x*- and *y*-axes of the image) is used for particle sizing. For a discussion of uncertainties in sizing of 2D-S particle images, see Appendix B of Lawson et al. (2008).

Although we do not expect significant contamination of the observations from particle shattering due to the generally small particle sizes observed in TTL cirrus (Korolev & Field, 2015), the FCDP arm tips and Hawkeye inlet tube have been designed to minimize the effects of shattered particles on the cloud microphysical observations. Postprocessing of the data further provides a degree of correction for the effects of shattering through analysis of particle interarrival times (Lawson, 2011).

The generally good agreement between the FCDP and 2D-S size distributions, as shown by the overlap in PSDs (particle size distributions) between 10 and 45 μm in the examples plotted in Figure 3, allows for combining the FCDP and 2D-S size distributions into a single combined size distribution, which are plotted in subsequent figures. The averaged size distributions plotted in Figure 3 were chosen to demonstrate the typical range of agreement of the overlap between the FCDP and 2D-S under varied conditions throughout the campaign. A scatter plot of total concentration over the size range of overlap (10–45 μm) for each instrument is plotted in Figure 4. The plot shows total concentration for 10-s averages to provide for higher FCDP counting statistics. Averaging over longer time periods, as is done for the results presented in this work, further collapses the scatter toward the solid line, which indicates a 1:1 ratio. Due to the larger uncertainties associated with the smaller bins of the 2D-S, differences in bin width, and counting statistics at lower concentrations, some scatter in agreement is expected, particularly across the smallest 2D-S bins. The apparent flat bottom of the scatter plot is due to the observation floor of the FCDP.

The single combined size distributions plotted in subsequent figures are the result of first independently averaging the 1-Hz FCDP and 2D-S size distributions over the appropriate temperature, altitude, or convective age observations. Due to differences in instrument operation, there are times where 1-Hz samples may only be available from one instrument; these observations are included in the instrument average. Once the individual instrument PSDs are averaged, a size cutoff for combining the FCDP and 2D-S average distributions is determined. This cutoff is chosen individually for each set of averaged PSDs by visually determining the point of intersection of the PSDs that yields the smoothest combined size distribution, generally around 30–40 μm in particle maximum size. Thus, the portion of the size distribution smaller than the cutoff is from FCDP observations (assuming circular area and spherical mass) and that larger than the cutoff from the 2D-S distributions (using the particle projected area for area and estimating mass from the area following Baker and Lawson, 2006).

The Hawkeye CPI is triggered by the 2D-S to record high (2.3 μm) resolution imagery of the particles, which is utilized for identifying ice particle habit. For each particle image, the particle focus, length, width, perimeter, area, and harmonics are determined, with a maximum uncertainty in sizing of in focus particles of about 5 μm (Lawson et al., 2008). These parameters are then used to auto-classify the particle images by habit. For this analysis, CPI images larger than 30 μm in diameter were auto-classified by habit into quasi-spheroids, columns, plates, rosettes, and budding rosettes following the classification criteria set forth in Lawson, Baker,

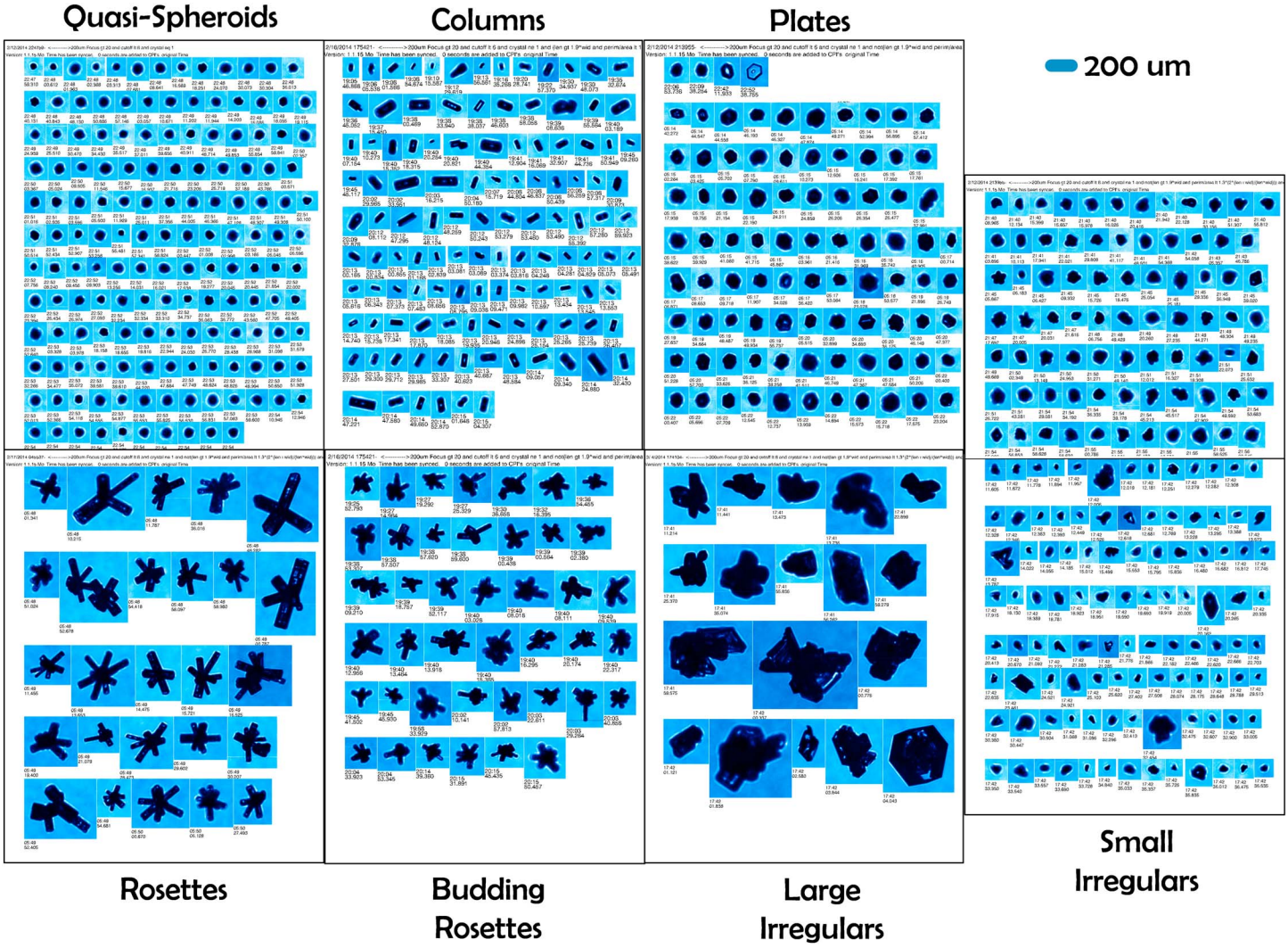

Figure 5. Example Hawkeye-cloud particle imager (CPI) images after auto-classification into quasi-spheroids, columns, plates, rosettes, budding rosettes, small and large irregulars and polycrystals.

Zmarzly, et al. (2006). Particles larger than 30 μm that cannot be classified into one of the habit categories are then separated into small (<200 μm) and large (>200 μm) irregulars, which includes polycrystals. An additional category is also used for CPI particles smaller than 30 μm in diameter, as at the small size of these images, budding rosettes or other habits begin to resemble quasi-spheroids and their small size precludes them from being easily classified. The term *quasi-spheroid* is utilized here in place of spheroid because the particles falling into this category are not perfectly spheroidal, but rather contain some irregularities on the surface. The finer surface structure of these particles could indicate the early formation stages of droxtals, budding Bucky balls, or "germ rosettes," but additional information regarding the fine surface scale of the particles is needed to make such distinction. Figure 5 shows sample image classification and also highlights the variability in the shape of the small and large irregulars.

Temperature and pressure measurements were provided by *Meteorological Measurement Systems* (Scott et al., 1990) at frequencies up to 20 Hz, and water vapor measurements were provided by the NOAA Water instrument (Thornberry et al., 2015) at a frequency of 1 Hz. The diode laser hygrometer also flew on the Global Hawk for ATTREX, and the agreement between the two water instruments was excellent (within a factor of 2), even at values less than 10 ppmv for TTL H_2O (Jensen et al., 2015). Relative humidity over ice, RHi, was computed from the 1-Hz *Meteorological Measurement Systems* and NOAA Water

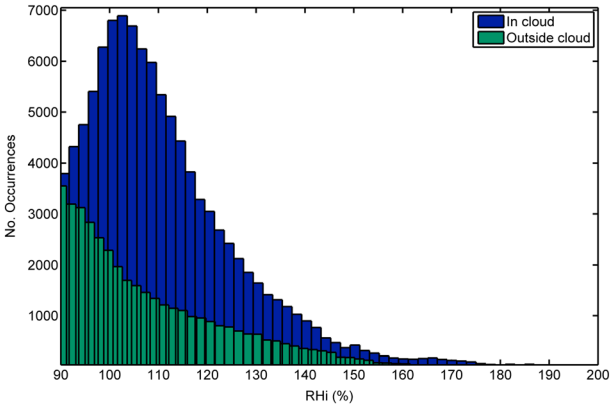

Figure 6. Frequency of occurrence of relative humidity with respect to ice in and out of cloud. RHi = relative humidity over ice.

observations using the vapor pressure over ice expressions provided by Murphy and Koop (2005). Figure 6 presents the frequency of occurrence of relative humidity with respect to ice in and out of cloud. Presence of cloud is determined by the 2D-S and FCDP concentration: when one or both instruments observe a total concentration exceeding 10 L^{-1}. Overall, observations of supersaturated air coincide with cloud occurrence approximately 72% of the time. Though observations in cloud extend to about 60–80% supersaturation, the mode of the distribution in supersaturation in cloud is approximately 3–5%, which is well within the ~10% uncertainty in the RHi measurement. Variability of RHi, as well as total concentration, with temperature is shown in Figure 7. Here the total concentration is computed from summing over a combined FCDP-2D-S concentration size distribution. Concentration and relative humidity 1-Hz measurements are averaged over 3°C temperature bins. Where higher concentrations occur, with ample particles competing for available water vapor, RHi tends to be near saturation (~100%). For regions with lower concentrations, where fewer crystals are competing for the available water vapor, higher values of relative humidity with respect to ice are observed, often at the colder temperatures (higher altitudes). The deviation from this pattern is found in the coldest temperature bin, where both higher RHi and higher concentration, resulting from nucleation near cloud top (Gallagher et al., 2012), are observed. Nucleation of this high concentration of particles rapidly drops the RHi below the critical level for nucleation, thus precluding the nucleation of additional particles. In the absence of the larger particles, the depositional growth rate is lower than what it would be for the population lower in the cloud, which contains more large particles. Once nucleated, this population of particles would take longer to reduce the RHi to near 100%, as it is at lower altitudes. Khvorostyanov et al. (2006) showed that due to slowed vapor absorption of these smaller particles, high ice supersaturations of 20–60% could persist on the order of several hours, with the supersaturation relaxation time increasing from a couple of hours at the cloud center to around 5–10 hr at the boundaries of the cloud.

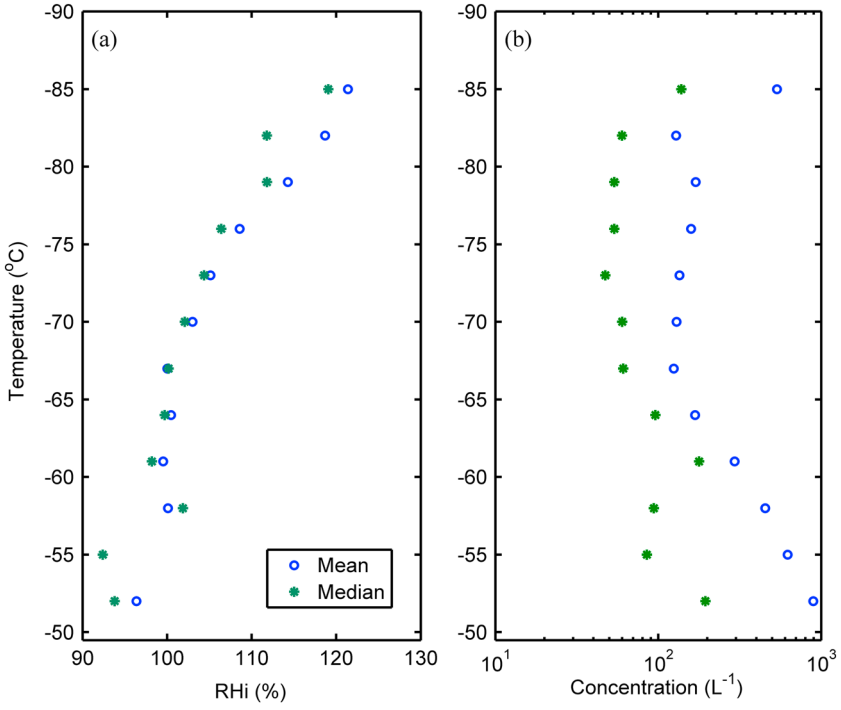

Figure 7. Average (a) relative humidity with respect to ice and (b) total concentration as a function of temperature. RHi = relative humidity over ice.

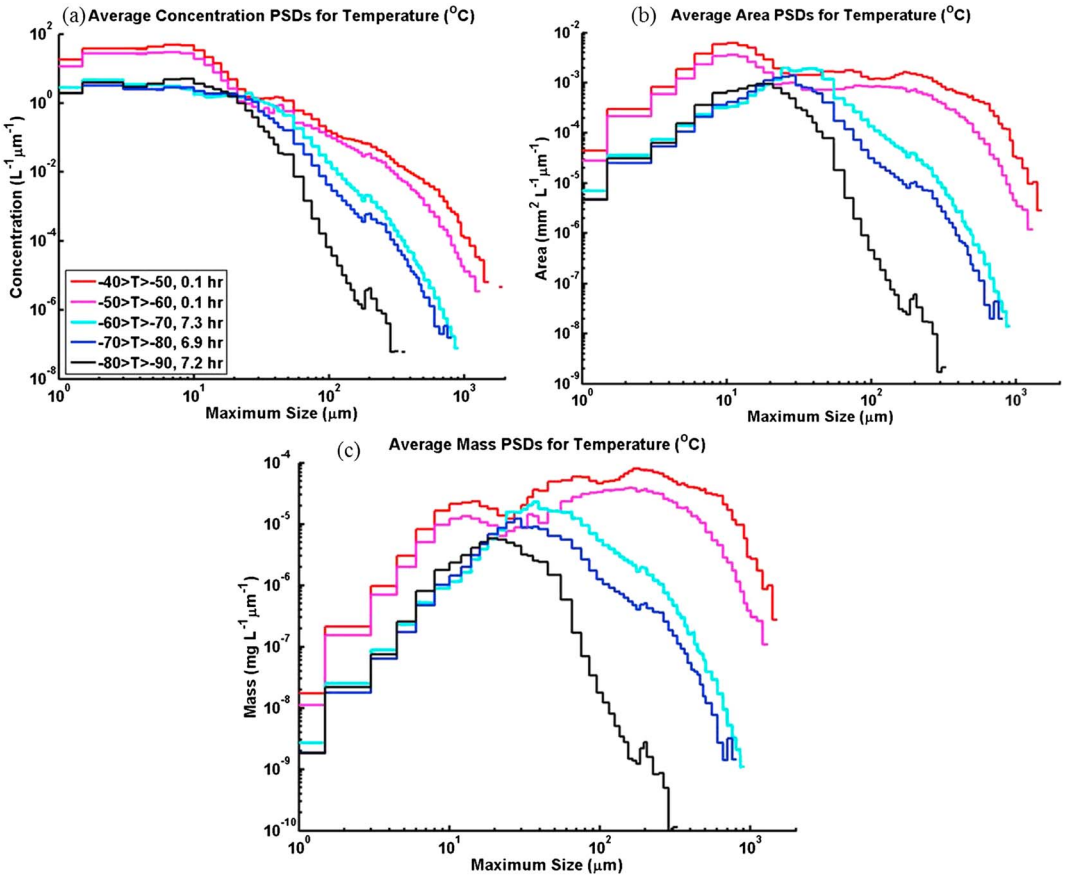

Figure 8. Average (a) concentration, (b) area, and (c) mass combined PSDs from the Fast Cloud Droplet Probe (maximum size less than about 35 μm) and Hawkeye-Two-Dimensional Stereo optical array probe (maximum size greater than about 35 μm) for different temperature (°C) regions.

3. Results

3.1. Size Distributions and Habits by Temperature

Cloud passes were segregated into 10°C temperature bins in order to examine variations in cloud microphysical characteristics as a function of temperature. Cloud passes were similarly separated into 1-km altitude ranges, and varying regions of estimated time since the air mass was convectively influenced (see section 3.3 on convective influence). Average concentration, area, and mass size distributions as well as percentages of CPI habits for these separations are presented below. As mentioned above, area size distributions are calculated assuming circular area for the small (less than ~30–40 μm) sizes observed by the FCDP and from the projected area of each particle for the larger sizes observed by the 2D-S. Similarly, the mass is calculated assuming spheres for the small sizes observed by the FCDP and estimated from the 2D-S projected area using the methodology described in Baker and Lawson (2006) for the larger sizes observed by the 2D-S.

Concentration PSDs from the FCDP and Hawkeye-2D-S for time periods where the number concentration in either instrument was nonzero (FCDP exceeded 4 L^{-1} and the 2D-S 0.01 L^{-1}) were averaged and combined into a single PSD for observations falling into each temperature region and are plotted in Figure 8. The breakpoint for combining PSDs between the two instruments was chosen for each temperature region based on the point or region of intersection of the individual instrument PSDs and was often around 30–40 μm. The sampling time over which the averages were computed is indicated in the figure legend. These plots show that the highest concentrations are found in the warmer temperature regions from −40 to −50°C and − 50 to −60 °C, with the breadth of the concentration distributions decreasing as the temperature regions get colder. Jackson et al. (2015) show similar size distributions from midlatitude cirrus observations separated

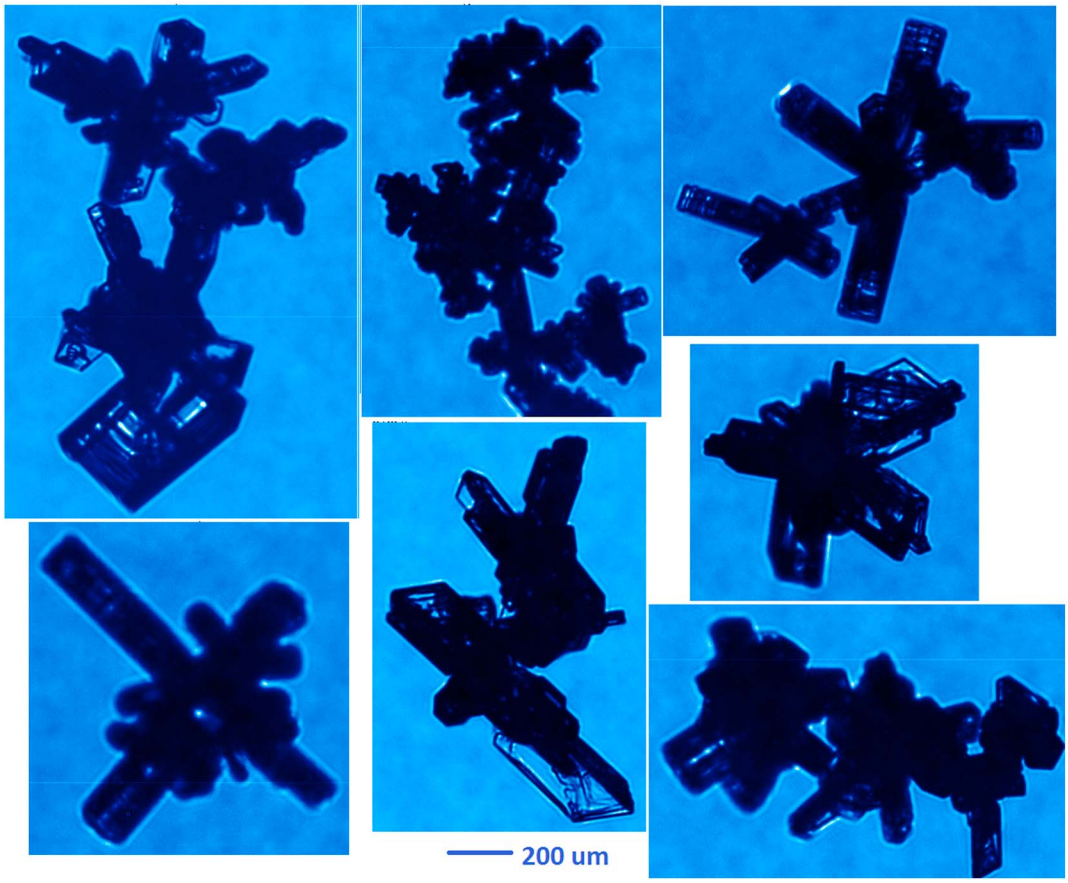

Figure 9. Example cloud particle imager images of the largest particles in the −40 to −60°C temperature region.

by temperature. These observations, taken between about −40 and −55°C, showed that the maximum size of the particles increased with temperature. Jackson et al. (2015) also noted higher concentrations of smaller particles were observed at lower temperatures in convective cirrus than in synoptic cirrus. In springtime midlatitude cirrus over the European continent, Luebke et al. (2016) also observed that, when separated by temperature, the concentration of small crystals decreased and the concentration of larger crystals increased with increasing temperature. It should be noted that the observations warmer than −60°C in the current analysis fall below the TTL (<13 km) and are limited to only 0.2 hr of data, as compared to around 7 hr of observations for each of the colder TTL temperature ranges; thus, the higher concentrations of small particles in Figure 8 are not statistically significant and may not be typical of small particle concentrations in this temperature range. It should also be noted that these sparse warmer observations below the TTL are, unlike the rest of the ATTREX data set, predominantly near convection, where particles extending to larger sizes would be expected. As shown in the example images of Figure 9, these larger particles are composed of aggregates, typical of convective influence, and large bullet rosettes, typical of in situ cirrus or cirrus regenerated from convective anvils. Aside from this small sample of aggregates, however, CPI images obtained during ATTREX contained very few aggregates, suggesting that aggregation is negligible in TTL cirrus.

Within the colder three temperature regions spanning −60 to −90°C, the concentration of the smaller sizes is of similar order of magnitude, but the largest sizes observed decrease with decreasing temperature, leading to a narrower distribution at the coldest temperatures. This trend is mirrored in the area and mass PSDs also plotted in Figure 8, where the PSDs for the coldest three temperature regions are of the same order of magnitude for particles smaller than 20 μm, but the area and mass PSDs of the warmer two temperature regions are much higher for these smaller particles. Since the distributions across the larger sizes increase in magnitude with increasing temperature, these trends produce a shift from a single mode mass PSD for the coldest three temperature regions into a bimodal mass PSD for the warmer two regions, with peaks

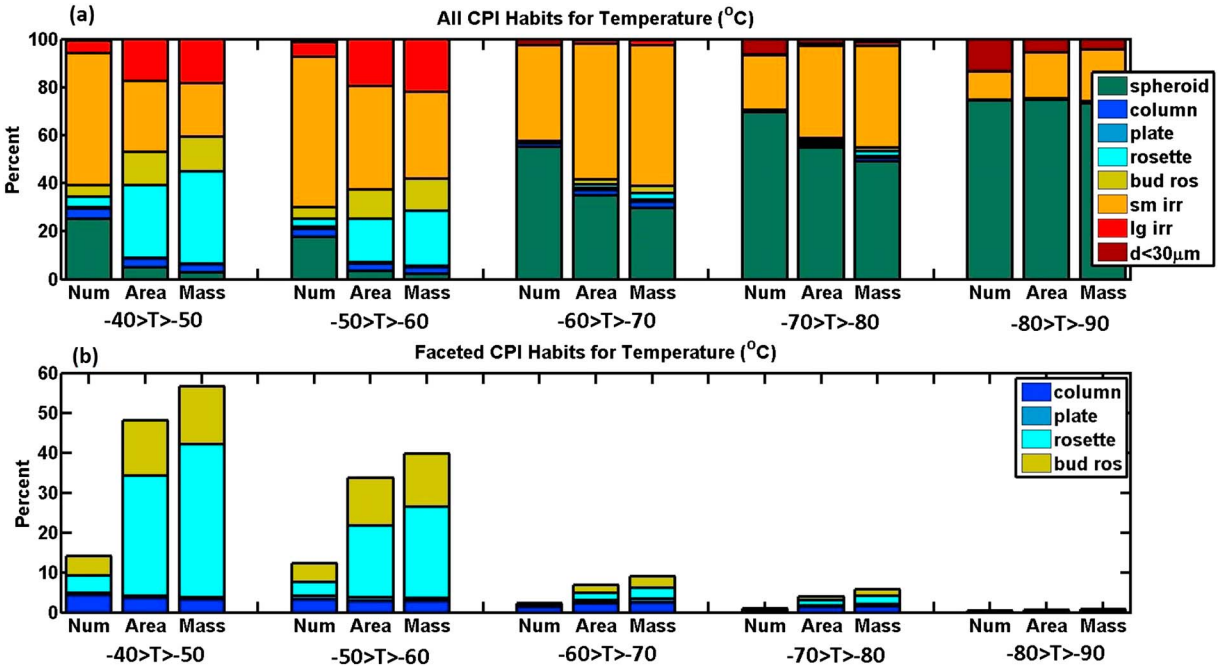

Figure 10. Percent of (a) all and (b) faceted ice particle habits by number, area, and mass observed by the Hawkeye-cloud particle imager (CPI) for the temperature ranges shown in Figure 8.

near 15 and 100–200 μm. The mode peak for the coldest three regions shifts to smaller sizes as the temperature decreases, moving from approximately 40 μm in the −60 to −70°C range to 30 μm for −70 to −80°C and 20 μm for −80 to −90°C.

The breakdown in classified particle habits by number, area, and mass from the Hawkeye-CPI for each of the temperature regions plotted above was also computed and is shown in Figure 10. Figure 10a shows the breakdown of all particles in each temperature region. Since the plot in Figure 10a is largely dominated by quasi-spheroids and small irregulars, the plot in Figure 10b is included to more distinctly show the breakdown of the faceted particles (columns, plates, rosettes, and budding rosettes). In this breakdown of habits by temperature, the number percentage of quasi-spheroids increases with decreasing temperature from just over 20% in the warmest regions to near 75% in the coldest region, with the three TTL temperature regions dominated by quasi-spheroidal particles. Quasi-spherical ice crystals, as indicated by relatively high lidar depolarization ratios, were also observed from the INCA (interhemispheric differences in cirrus cloud properties by anthropogenic emissions) experiment over Patagonia (Immler & Schrems, 2002). Observations from INCA suggest that cirrus formed during the experiment were associated with homogeneous nucleation (Gayet et al., 2004; Immler & Schrems, 2002). The population of particles smaller than 30 μm similarly increases with respect to the other particle habits with decreasing temperature. The prevalent dominance of the particle population by quasi-spheroids has potentially far-reaching implications for the radiative properties of TTL cirrus. Though the CPI images cannot distinguish the small-scale surface roughness of the crystals, measurements by instruments such as SID3 have shown that the scattering properties of rounded particles varies from that of faceted or rougher irregular particles (Mishchenko et al., 1996; Ulanowski et al., 2006). These scattering properties can strongly influence the net radiative forcing of cirrus clouds, which play an important role in the Earth-atmosphere radiation balance (Baran, 2009; Wendisch et al., 2007, and references therein). Based on a single scattering property database with six ice particle habits and assumedly smooth surfaces, Hong et al. (2009) used simulations to show that for optically thick clouds, large differences in shortwave occurred, and for clouds with small effective diameters, large differences occurred in the longwave. Roughening of the surface of the particles, as well as complex morphologies to the crystal structure will furthermore affect the single scattering properties of the particles, but the extent to which these parameters will affect the radiative properties is still a complex question in need of further investigation (Yang et al., 2015).

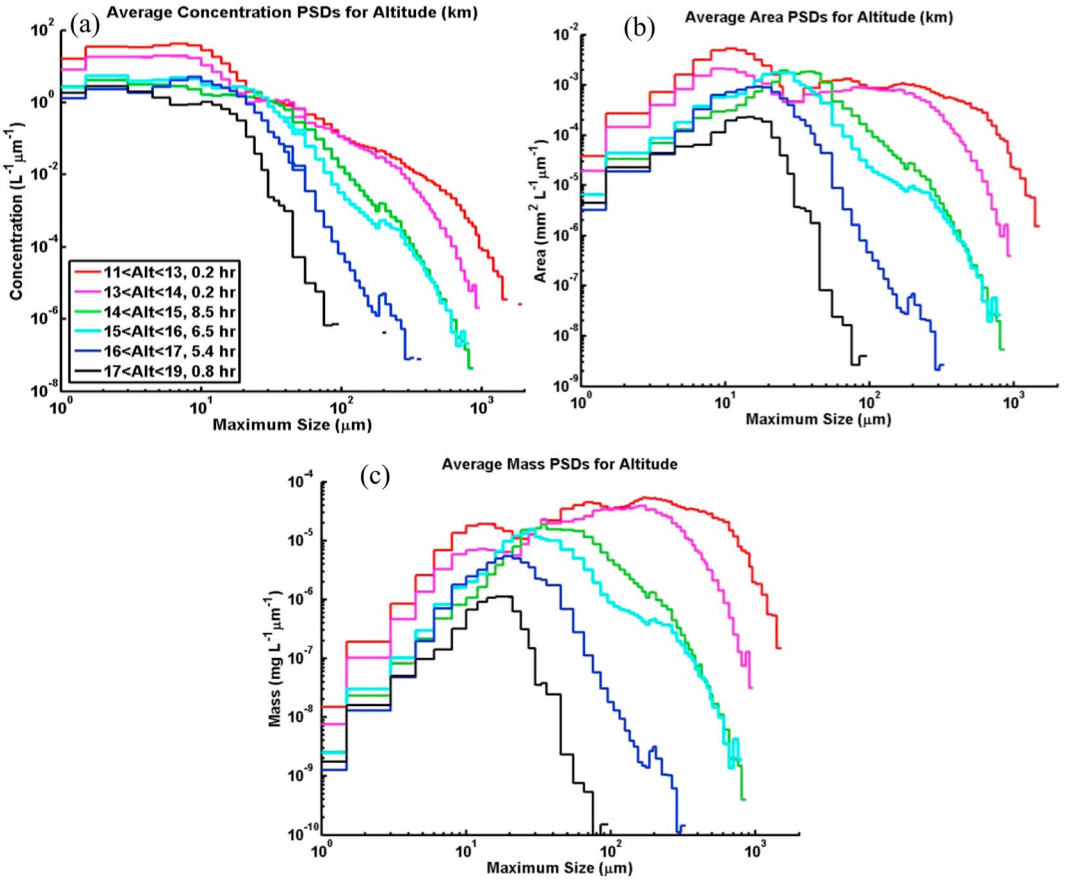

Figure 11. Average (a) concentration, (b) area, and (c) mass combined PSDs from the Fast Cloud Droplet Probe and Hawkeye-Two-Dimensional-Stereo optical array probe for regions of altitude (km).

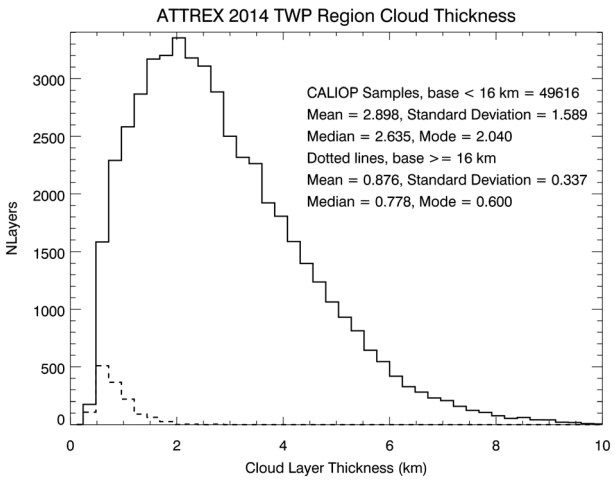

Figure 12. CALIOP TTL mean cloud thickness during February–March 2014 for clouds with a base below 16 km and a top exceeding 14.5 km, and the mean cloud thickness for clouds with a base above 16 km. ATTREX = Airborne Tropical TRopopause EXperiment; CALIOP = Cloud-Aerosol Lidar with Orthogonal Polarization; TTL = tropical tropopause layer.

The other particle habits, both faceted and irregulars increase in percentage of occurrence by number, area, and mass from the coldest to warmest temperatures. In the warmer two regions, which contain larger percentages of faceted habits, these habits are dominated by the combination of rosettes and budding rosettes, in agreement with previous CPI observations of cirrus generated in situ by Lawson, Baker, Pilson, et al. (2006). The dominance of rosettes is particularly noticeable in percentage of occurrence by area and mass due to the larger sizes of rosettes compared with other shapes. Rosette shapes (polycrystals) are almost exclusively found in cirrus formed in situ (Connolly et al., 2005; Lawson et al., 2003, 2010; Whiteway et al., 2004). This suggests that the polycrystals and aggregates in Figure 10 were formed in situ, not in updrafts of convection. This proposition is supported by the fact that very few aggregates were observed in the colder TTL particle images. Similarly, the trend showing higher percentages of larger, faceted crystals at warmer temperatures in Figure 8, suggests diffusional growth as particles descend through warmer regions of cloud.

3.2. Size Distributions and Habits by Altitude

Since there is a strong correlation of temperature with altitude in the regions sampled, the breakdown of average size distributions into altitude regions, shown in Figure 11, expectedly have a similar trend to

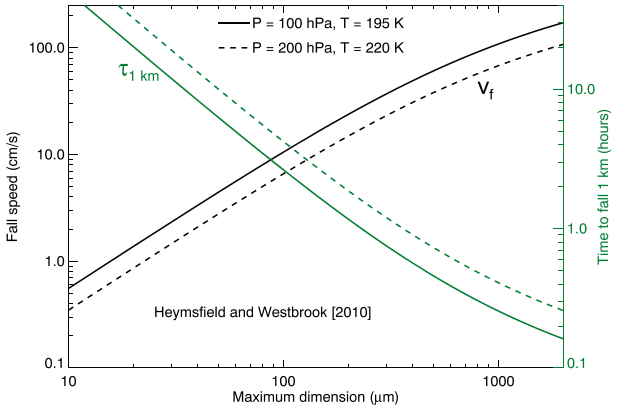

Figure 13. Ice crystal terminal fallspeeds and corresponding time to fall 1 km.

the breakdown by temperature shown in Figure 8: The lower altitudes have broader concentration, area, and mass size distributions, which narrow with increasing altitude. However, the distributions at the highest altitudes are narrower than when separated by temperature. The particle habits similarly contain a larger percentage of faceted habits in the lowest altitudes, where the combination of rosettes and budding rosettes again dominates the habit makeup of the area and mass distributions. The habit breakdown is so similar that it is difficult to distinguish differences; thus, the plot is not shown. Figure 12 shows the distribution of TTL cloud thickness observed by the Cloud-Aerosol Lidar with Orthogonal Polarization (CALIOP) during the ATTREX February to March 2014 time frame. CALIOP is a dual-wavelength, polarization-sensitive lidar onboard the CALIPSO satellite. Since the tail of the cloud particle concentration size distributions falls off more rapidly across the larger sizes at altitudes above 16 km than those below 16 km, two distributions of CALIOP cloud thickness are presented for comparison: the mean cloud thickness for clouds with a base below 16 km and the mean cloud thickness for clouds with a base above 16 km. The clouds with bases above 16 km are geometrically thinner than those at the lower altitudes, with the higher clouds having a mean cloud thickness of about 0.876 km and a maximum cloud depth of about 2 km. These clouds are expectedly narrow in depth because their tops do not rise above the cold-point tropopause. The lower clouds have a mean depth of 2.898 km, with some extending to nearly 10 km in thickness. Given the depth of these clouds, the broader size distributions at the lower

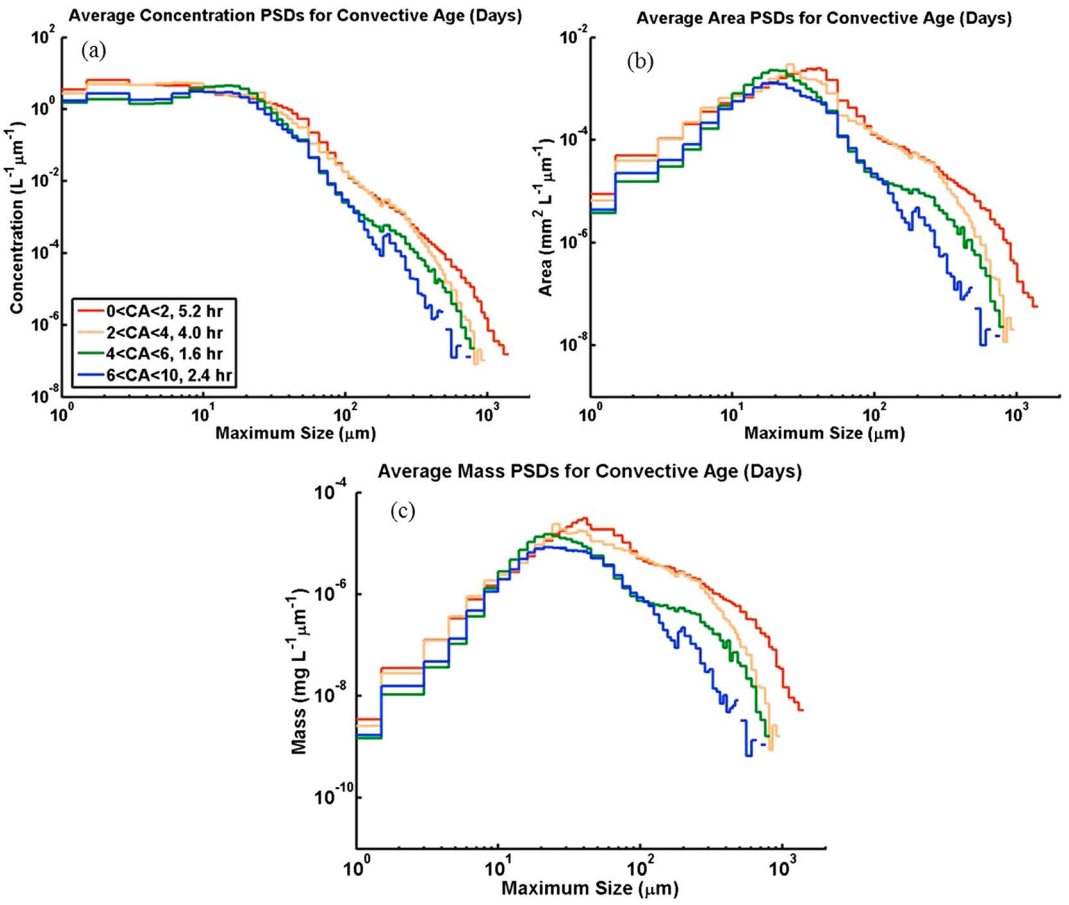

Figure 14. Average (a) concentration, (b) area, and (c) mass combined PSDs from the Fast Cloud Droplet Probe and Hawkeye-two-dimensional stereo optical array probe for regions of age since convective influence (CA; days).

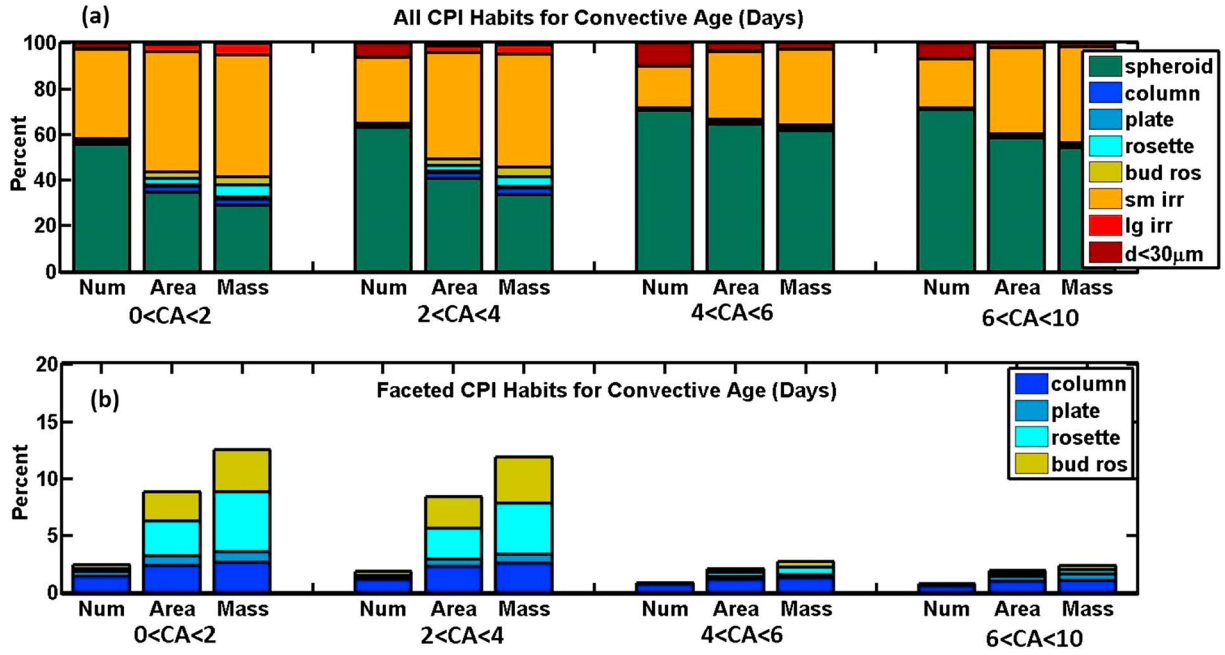

Figure 15. Percent of (a) all and (b) faceted ice particle habits observed by number, area, and mass by the Hawkeye-cloud particle imager (CPI) for the regions of age since convective influence shown in Figure 14.

altitudes suggest both gravitational size sorting (sedimentation of larger crystals toward the lower parts of the cloud) and growth of the larger particles as they sediment into regions of increasing RHi and increasing temperature at lower altitudes, which is again consistent with the relative increase in occurrence of the rosettes and large irregulars at the lower altitudes and warmer temperatures.

3.3. Size Distributions and Habits by Age Since Convection

As mentioned above, ice crystals detrained directly from deep convection were rarely sampled during ATTREX, rather the majority of observations are likely cirrus formed in situ, or new growth of detrained particles from earlier convection that were advected into a region with relatively high humidity. Figure 13 shows ice crystal terminal fallspeeds and the corresponding time to fall 1 km calculated using bullet rosette mass dimensional relationships (Heymsfield & Westbrook, 2010; Mitchell & Heymsfield, 2005; Westbrook, 2008). The ice crystals with a maximum dimension approaching 1 mm will fall out of the TTL in less than an hour, while the time for the longer-suspended population of particles smaller than 30 μm to fall 1 km is on the order of half of a day. Thus, it is very likely that once beyond a convective age of a few days, the original ice crystals would have sedimented or sublimated after entering a region of lower supersaturation, since ice crystals larger than about 100 μm will fall out of the TTL within a few hours.

The breakdown of average size distributions and habit percentages into periods of age since convective influence is shown in Figures 14 and 15. The age since convective influence is estimated by running several clusters of back trajectories from different points along the flight track. Each trajectory cluster includes 25 trajectories run from a range of latitude, longitude, and potential temperature, θ, values centered on flight track locations that are about a quarter degree apart. ERA Interim winds with 0.75° resolution (every 6 hr) are used. Since model level analyses are used, the effective vertical resolution near the tropopause is about 1 km. For each trajectory, the number of days since the most recent convection is calculated by running each trajectory through 3-hourly fields of cloud top potential temperatures. The cloud top potential temperature fields are based on TRMM/Microwave/IR rainfall information, global IR brightness temperature information from geostationary satellites, and ERA-Interim model level temperature analyses (see Bergman et al., 2012 for further details). Convective influence is said to occur if the trajectory point comes within 0.25° of a point where the cloud top theta is greater than or equal to the trajectory theta (Bergman et al., 2012).

The most noticeable difference in the size distributions separated by age since convection occurs in the most recently influenced air mass, where the cloud particle population contains higher concentrations of larger ice particles. These particles could be of liquid origin (Krämer et al., 2016; Luebke et al., 2016), however, were these large particles detrained from deep convection, they would sediment out of the TTL on the timescale of one to a few hours, as demonstrated by the fallspeeds shown in Figure 13. Were these large particles detrained from deep convection, we would also expect to see a larger percentage of aggregates in the population. However, few aggregates, if any, are observed. As shown in Figure 14, larger ice particles are observed sometimes days after the air mass has been convectively influenced. It should be noted that there is a slight correlation of increasing convective age with increasing altitude, but the trend observed in Figure 14 persists when further restricting the observations by additional altitude constraints. This higher concentration of larger particles could be due to multiple influences, including (1) a region of high relative humidity (RHi $>$ 100%), resulting from convection near where these clouds were sampled; (2) gravity waves that are often generated in the upper troposphere as a result of the blocking influence of convection (Kim et al., 2016; Kim & Alexander, 2015); (3) other synoptic or mesoscale influences that caused widespread lifting and increased RHi (Ueyama et al., 2015); and (4) the product of heterogeneous nucleation on effective INP recently injected by active deep convection. Effective INP (ice nucleating particles), nucleating at lower supersaturation than required for homogeneous nucleation, would scavenge available water vapor, growing in situ to larger sizes.

Beyond about 4 days since convective influence, average size distributions for the regions with longer times since convective influence are very similar in magnitude and shape, with only a slight decrease in concentration of the largest particles with increasing time since convection, likely due to fallout of larger particles via sedimentation. It is interesting to note that while one would expect the number of smaller particles to decrease from aggregation in the proximity of deep convection, entrainment, and evaporation, the concentration of smaller particles remains relatively the same, likely due to new ice crystal nucleation. If the ice crystals are generally nucleated in situ, that is, not in the convective updrafts, then a dependence of small particle concentration on age since convective influence would not be expected. Past a few days of convective influence then, the observed ice crystals were nucleated in situ, and in this case the age since convection probably has little to do with the age of the cloud itself, rather it is related to the air mass that was influenced by the convection. Again, ATTREX flights generally avoided sampling near deep convection, so these observations are not suitable for examining the properties of anvil cirrus.

Correspondingly, the breakdown of habits by age since convective influence, Figure 15, shows a slightly higher percentage of faceted particles in the observations most recently influenced by convection, though they occur in much lower percentages than when separated by temperature or altitude. The percentage of faceted habits decreases with increasing time since convective influence, likely due to fallout of the larger faceted habits and/or sublimation of the faceted edges as well as constraint in maximum size induced by ambient moisture levels downwind of convection. The average percentage of spheroids dominates the habits by number irrespective of age since convective influence and by area and mass for observations that have not recently undergone convective influence. On the other hand, small irregulars dominate the area and mass distributions in the observations that have undergone convective influence more recently, likely because they have not undergone sublimation that tends to reduce their shape to quasi-spherical (Jarvinen et al., 2016; Korolev & Isaac, 2003). Though the concentration, area, and mass size distributions continue to decrease across the larger sizes with increasing time since convection, there is little further change in the breakdown by habit past about 5 days since convective influence.

4. Summary

Though the moisture required for crystal growth may have come from convection, ATTREX provided ample sampling of mostly aged in situ grown cirrus. As seen in Figures 8–15, the observed size distributions contained the highest concentrations of larger ($>$50 μm) particles in the warmer temperature regions and lower altitudes, demonstrated by broader concentration and mass size distributions. Similarly to the particle habits observed by Lawson et al. (2008), the ice particles were predominantly quasi-spheroidal in shape, followed by small irregulars. The large percentage of quasi-spheroidal particles increases with decreasing temperature and increasing altitude. The percent of quasi-spheroids also increases when moving from very recent

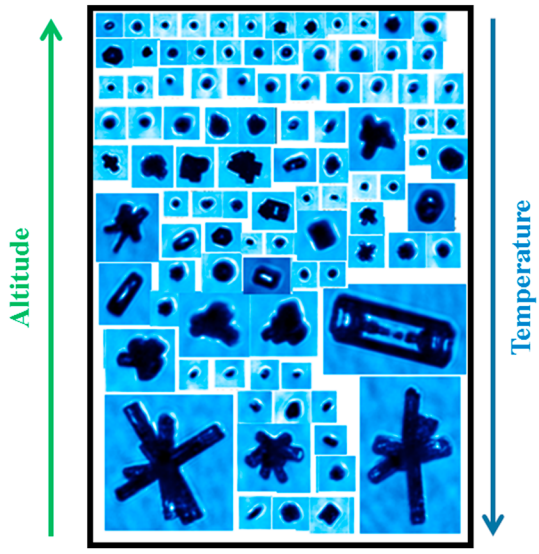

Figure 16. Schematic of sample cloud particle imager images showing example structure of tropical tropopause layer in situ cirrus: Smaller particles are observed throughout the vertical extent of the cloud, but with the highest concentration of smallest particles near cloud top. Maximum size of particles increases at lower altitudes (warmer temperatures).

convective influence out to about 5 days, then it shows little variation with further increasing age since convective influence. The percentage of smallest (<30 μm) particles, which are too small to clearly identify by particle habit in the CPI images, shows similar trends to the quasi-spheroidal particles: These small particles increase in percentage with decreasing temperature, increasing altitude, and with increasing time since convective influence. The prevalent dominance of the particle population by quasi-spheroids has potentially far-reaching implications for the radiative properties of TTL cirrus because the scattering properties of rounded particles vary significantly from that of faceted or irregular particles and can lead to significant radiative heating. These pervasive thin cirrus clouds reflect solar radiation and absorb thermal infrared emission from the Earth's surface and lower atmosphere. Though smoother in shape than their faceted and irregular counterparts, these quasi-spheroids may still contain surface structure that causes their scattering properties to differ from that of a smooth sulfate aerosol, however, and additional investigation to characterize the surface roughness of these particles is still needed.

In comparison to the large population of quasi-spheroids, which could be interpreted as germ rosettes, the faceted habits (columns, plates, rosettes, and budding rosettes) were typically found in lower percentages but were found in higher percentages at lower altitudes and warmer temperatures than when separated by a metric for the age since the air parcel underwent convective influence. This percentage of faceted habits, as well as the percentage of irregulars, demonstrated an inverse trend to that of the quasi-spheroids: The faceted habits decreased in percentage with decreasing temperature, increasing altitude, and with increasing time since convective influence. The trend showing higher percentages of faceted crystals at warmer temperatures demonstrates diffusional growth as particles descend through cloud, and/or the more rapid diffusional growth rate at warmer temperatures. The sparsity of aggregates in the CPI images obtained during ATTREX strongly suggests that particle aggregation is negligible in TTL cirrus.

The schematic in Figure 16 pictorially shows an example structure of TTL in situ cirrus: Smaller particles are observed throughout the vertical extent of the cloud, but with the highest concentration of smallest particles near cloud top, near the cold-point tropopause. In the life cycle of these TTL cirrus, convection brings up moisture and ice, which is detrained. The larger particles will fall out, and the smaller detrained particles will sublimate or continue to grow in situ depending on the environment. Within the cirrus cloud, as the particles settle into warmer temperatures, they grow via vapor deposition, with negligible aggregation, so that the maximum size of particles increases at lower altitudes (warmer temperatures), provided ample saturation conditions exist, as was often the case during ATTREX. Larger ice crystals are quickly removed from the TTL by sedimentation, and fall out, while the smaller ice can survive for several hours. The air mass travels downstream, hits a cold pool, and forms or regrows any surviving crystals in situ via waves, radiatively driven events, moderately small increases in relative humidity, and so forth. Through these processes, growth-sedimentation is dominant in determining TTL cirrus size distributions and habits. Additional analysis would benefit from TTL cirrus microphysical measurements obtained in different seasons, from additional regions, and from additional observations at colder temperatures, as well as observations of anvil cirrus close to deep convection.

Acknowledgments
The authors acknowledge funding from NASA Airborne Tropical Tropopause EXperiment under contract NNA10DF71C. The data used in this analysis are available in the NASA ESPO database at https://espoarchive.nasa.gov/archive/browse/attrex/id4.

References

Bailey, M., & Hallett, J. (2009). A comprehensive habit diagram for atmospheric ice crystals: Confirmation from the laboratory, AIRS II, and other field studies. *Journal of Atmospheric Science*, *66*(9), 2888–2899. https://doi.org/10.1175/2009JAS2883.1

Baker, B., & Lawson, R. P. (2006). Improvement in determination of ice water content from two-dimensional particle imagery: Part I: Image to mass relationships. *Journal of Applied Meteorology*, *45*(9), 1282–1290. https://doi.org/10.1175/JAM2398.1

Baran, A. J. (2009). A review of the light scattering properties of cirrus. *Journal of Quantitative Spectroscopy & Radiative Transfer*, *110*(14-16), 1239–1260. https://doi.org/10.1016/j.jqsrt.2009.02.026

Bergman, J. W., Jensen, E. J., Pfister, L., & Yang, Q. (2012). Seasonal differences of vertical-transport efficiency in the tropical tropopause layer: On the interplay between tropical deep convection, large-scale vertical ascent, and horizontal circulations. *Journal of Geophysical Research*, *117*, D05302. https://doi.org/10.1029/2011JD016992

Comstock, J. M., Ackerman, T. P., & Mace, G. G. (2002). Ground based remote sensing of tropical cirrus clouds at Nauru Island: Cloud statistics and radiative impacts. *Journal of Geophysical Research*, *107*(D23), 4714. https://doi.org/10.1029/2002JD002203

Connolly, P. J., Saunders, C. P. R., Gallagher, M. W., Bower, K. N., Flynn, M. J., Choularton, T. W., et al. (2005). Aircraft observations of the influence of electric fields on the aggregation of ice crystals. *Quarterly Journal of the Royal Meteorological Society*, *131*(608), 1695–1712. https://doi.org/10.1256/qj.03.217

Davis, S., Hlavka, D., Jensen, E., Rosenlof, K., Yang, Q., Schmidt, S., et al. (2010). In situ and lidar observations of tropopause subvisible cirrus clouds during TC4. *Journal of Geophysical Research*, *115*, D00J17. https://doi.org/10.1029/2009JD013093

Forster, P. M. F., & Shine, K. P. (2002). Assessing the climate impact of trends in stratospheric water vapor. *Geophysical Research Letters*, *29*(6), 1086. https://doi.org/10.1029/2001GL013909

Gallagher, M. W., Connolly, P. J., Heymsfield, A., Bower, K. N., Choularton, T. W., Allen, G., et al. (2012). Observations and modelling of microphysical variability, aggregation and sedimentation in tropical anvil cirrus outflow regions. *Atmospheric Chemistry and Physics*, *12*(14), 6609–6628. https://doi.org/10.5194/acp-12-6609-2012

Gayet, J.-F., Ovarlez, J., Shcherbakov, V., Ström, J., Schumann, U., Minikin, A., et al. (2004). Cirrus cloud microphysical and optical properties at southern and northern midlatitudes during the INCA experiment. *Journal of Geophysical Research*, *109*, D20206. https://doi.org/10.1029/2004JD004803

Haladay, T., & Stephens, G. (2009). Characteristics of tropical thin cirrus clouds deduced from joint CloudSat and CALIPSO observations. *Journal of Geophysical Research*, *114*, D00A25. https://doi.org/10.1029/2008JD010675

Heymsfield, A. J. (1986). Ice particles observed in a cirriform cloud at −83 °C and implications for polar stratospheric clouds. *Journal of Atmospheric Science*, *43*(8), 851–855. https://doi.org/10.1175/1520-0469(1986)043%3C0851:IPOIAC%3E2.0.CO;2

Heymfsield, A. J., & Westbrook, C. D. (2010). Advances in the Estimation of Ice Particle Fall Speeds Using Laboratory and Field Measurements. *Journal of the Atmospheric Sciences*, *67*, 2469–2482. https://doi.org/10.1175/2010JAS3379.1

Hong, G., Yang, P., Baum, B. A., Heymsfield, A. J., & Xu, K.-M. (2009). Parameterization of shortwave and longwave radiative properties of ice clouds for use in climate models. *Journal of Climate*. *22*, 6287–6312.

Immler, F., & Schrems, O. (2002). LIDAR measurements of cirrus clouds in the northern and southern midlatitudes during INCA (55N, 53S): A comparative study. *Geophysical Research Letters*, *29*(16), 1809. https://doi.org/10.1029/2002GL015077

Jackson, R. C., McFarquhar, G. M., Fridlind, A. M., & Atlas, R. (2015). The dependence of cirrus gamma size distributions expressed as volumes in N0-λ-μ phase space and bulk cloud properties on environmental conditions: Results from the Small Ice Particles in Cirrus Experiment (SPARTICUS). *Journal of Geophysical Research: Atmospheres*, *120*, 10,351–10,377. https://doi.org/10.1002/2015JD023492

Jarvinen, E., Schnaiter, M., Mioche, G., Jourdan, O., Shcherbakov, V. N., Costa, A., et al. (2016). Quasi-spherical ice in convective clouds. *Journal of Atmospheric Science*, *73*(10), 3885–3910. https://doi.org/10.1175/JAS-D-15-0365.1

Jensen, E. J., Diskin, G., Paul Lawson, R., Lance, S., Paul Bui, T., Hlavka, D., et al. (2013a). Ice nucleation and dehydration in the tropical tropopause layer. *Proceedings of the National Academy of Science*, *110*(6), 110. https://doi.org/10.1073/pnas.1217104

Jensen, E. J., Diskin, G., Paul Lawson, R., Lance, S., Paul Bui, T., Hlavka, D., et al. (2013b). The NASA Airborne Tropical TRopopause EXperiment (ATTREX). *SPARC Newsletter*, *41*, 15–24.

Jensen, E. J., Pfister, L., Bui, T. V., Lawson, P., Baker, B., Mo, Q., et al. (2008). Formation of large (≈100 μm) ice crystals near the tropical tropopause. *Atmospheric Chemistry and Physics*, *8*(6), 1621–1633. https://doi.org/10.5194/acp-8-1621-2008

Jensen, E. J., Pfister, L., Jordan, D. E., Bui, T. V., Ueyama, R., Singh, H. B., et al. (2015). The NASA Airborne Tropical TRopopause EXperiment (ATTREX): High-altitude aircraft measurements in the Tropical Western Pacific. *Bulletin of the American Meteorological Society*, *98*(1), 129–143. https://doi.org/10.1175/BAMS-D-14-00263.1

Jensen, E. J., Ueyama, R., Pfister, L., Bui, T. V., Lawson, P., Woods, S., et al. (2016). On the susceptibility of cold tropical cirrus to ice nuclei abundance. *Journal of Atmospheric Science*, *73*(6), 2445–2464. https://doi.org/10.1175/jas-d-15-0274.1

Khvorostyanov, V. I., Morrison, H., Curry, J. A., Baumgardner, D., & Lawson, P. (2006). High supersaturation and modes of ice nucleation in thin tropopause cirrus: Simulation of the 13 July 2002 Cirrus Regional Study of Tropical Anvils and Cirrus Layers case. *Journal of Geophysical Research*, *111*, D02201. https://doi.org/10.1029/2004JD005235

Kim, J.-E., & Alexander, M. J. (2015). Direct impacts of waves on tropical cold point tropopause temperature. *Geophysical Research Letters*, *42*, 1584–1592. https://doi.org/10.1002/2014GL062737

Kim, J.-E., Alexander, J. M., Bui, P. T., Dean-Day, J. M., Lawson, P., Woods, S., et al. (2016). Ubiquitous influence of waves on tropical high cirrus cloud. *Geophysical Research Letters*, *43*(11), 5895–5901. https://doi.org/10.1002/2016gl069293

Korolev, A., & Field, P. R. (2015). Assessment of the performance of the inter-arrival time algorithm to identify ice shattering artifacts in cloud particle probe measurements. *Atmospheric Measurement Technology*, *8*(2), 761–777. https://doi.org/10.5194/amt-8-761-2015

Korolev, A., & Isaac, G. (2003). Roundness and aspect ratio of particles in ice clouds. *Journal of Atmospheric Science*, *60*(15), 1795–1808. https://doi.org/10.1175/1520-0469(2003)060%3C1795:RAAROP%3E2.0.CO;2

Korolev, A. V. (2007). Reconstruction of the sizes of spherical particles from their shadow images. Part I: Theoretical considerations. *Journal of Atmospheric and Oceanic Technology*, *24*(3), 376–389. https://doi.org/10.1175/JTECH1980

Krämer, M., Rolf, C., Luebke, A., Afchine, A., Spelten, N., Costa, A., et al. (2016). A microphysics guide to cirrus clouds—Part 1: Cirrus types. *Atmospheric Chemistry and Physics*, *16*(5), 3463–3483. https://doi.org/10.5194/acp-16-3463-2016

Lawson, P., Baker, B. A., & Pilson, B. L. (2003). *In situ measurements of microphysical properties of mid-latitude and anvil cirrus and validation of satellite retrievals*. Paper presented at 30th International Symposium on Remote Sensing of Environment, Honolulu, Hawaii.

Lawson, R. P. (2011). Effects of ice particles shattering on the 2D-S probe. *Atmospheric Measurement Technology*, *4*(7), 1361–1381. https://doi.org/10.5194/amt-4-1361-2011

Lawson, R. P., Baker, B., Zmarzly, P., O'Connor, D., & Mo, Q. (2006). Microphysical and optical properties of atmospheric ice crystals at South Pole Station. *Journal of Applied Meteorology and Climate*, *45*(11), 1505–1524. https://doi.org/10.1175/JAM2421.1

Lawson, R. P., Baker, B. A., Pilson, B., & Mo, Q. (2006). In situ observations of the microphysical properties of wave, cirrus and anvil clouds. Part II: Cirrus clouds. *Journal of Atmospheric Science*, *63*(12), 3186–3203. https://doi.org/10.1175/JAS3803.1

Lawson, R. P., Baker, B. A., Schmitt, C. G., & Jensen, T. L. (2001). An overview of microphysical properties of Arctic stratus clouds observed during FIRE.ACE. *Journal of Geophysical Research*, *106*(D14), 14,989–15,014. https://doi.org/10.1029/2000JD900789

Lawson, R. P., Gurganus, C., & Woods, S. (2017). Aircraft observations of cumulus microphysics ranging from the tropics to mid-latitudes: Implications for a "new" secondary ice process. *Journal of Atmospheric Science*, *74*(9), 2899–2920. https://doi.org/10.1175/JAS-D-17-0033.1

Lawson, R. P., Jensen, E., Mitchell, D. L., Baker, B., Mo, Q., & Pilson, B. (2010). Microphysical and radiative properties of tropical clouds investigated in TC4 and NAMMA. *Journal of Geophysical Research*, *115*, D00J08. https://doi.org/10.1029/2009JD013017

Lawson, R. P., O'Connor, D., Zmarzly, P., Weaver, K., Baker, B., & Mo, Q. (2006). The 2D-S (stereo) probe: Design and preliminary tests of a new airborne high-speed. High-resolution particle imaging probe. *Journal of Atmospheric and Oceanic Technology*, *23*(11), 1462–1477. https://doi.org/10.1175/JTECH1927.1

Lawson, R. P., Pilson, B., Baker, B., Mo, Q., Jensen, E., Pfister, L., & Bui, P. (2008). Aircraft measurements of microphysical properties of subvisible cirrus in the tropical tropopause layer. *Atmospheric Chemistry and Physics*, *8*(6), 1609–1620. https://doi.org/10.5194/acp-8-1609-2008

Luebke, A. E., Afchine, A., Costa, A., Grooß, J.-U., Meyer, J., Rolf, C., et al. (2016). The origin of midlatitude ice clouds and the resulting influence on their microphysical properties. *Atmospheric Chemistry and Physics*, *16*(9), 5793–5809. https://doi.org/10.5194/acp-16-5793-2016

McFarquhar, G. M., Heymsfield, A. J., Spinhirne, J., & Hart, B. (2000). Thin and subvisual tropopause tropical cirrus: Observations and radiative impacts. *Journal of Atmospheric Science*, *57*(12), 1841–1853. https://doi.org/10.1175/1520-0469(2000)057%3C1841:TASTTC%3E2.0.CO;2

Mishchenko, M. I., Rossow, W. B., Macke, A., & Lacis, A. A. (1996). Sensitivity of cirrus cloud albedo, bidirectional reflectance, and optical thickness retrieval accuracy to ice-particle shape. *Journal of Geophysical Research*, *101*(D12), 16,973–16,985. https://doi.org/10.1029/96JD01155

Mitchell, D., & Heymsfield, A. (2005). Refinements in the treatment of ice particle terminal velocities, highlighting aggregates. *Journal of Atmospheric Science*, *62*(5), 1637–1644. https://doi.org/10.1175/JAS3413.1

Murphy, D. M., & Koop, T. (2005). Review of the vapour pressures of ice and supercooled water for atmospheric applications. *Quarterly Journal of the Royal Meteorological Society*, *131*(608), 1539–1565. https://doi.org/10.1256/qj.04.94

Riese, M., Ploeger, F., Rap, A., Vogel, B., Konopka, P., Dameris, M., & Forster, P. (2012). Impact of uncertainties in atmospheric mixing on simulated UTLS composition and related radiative effects. *Journal of Geophysical Research*, *117*, D16305. https://doi.org/10.1029/2012JD017751

Rollins, A. W., Thornberry, T. D., Gao, R. S., Woods, S., Lawson, R. P., Bui, T. P., et al. (2016). Observational constraints on the efficiency of dehydration mechanisms in the tropical tropopause layer. *Geophysical Research Letters*, *43*, 2912–2918. https://doi.org/10.1002/2016GL067972

Schoeberl, M., Jensen, E., & Woods, S. (2015). Gravity waves amplify upper tropospheric dehydration by clouds. *Earth and Space Science*, *2*(12), 485–500. https://doi.org/10.1002/2015EA000127

Scott, S. G., Paul Bui, T., & Roland Chan, K. (1990). The meteorological measurement system on the NASA ER-2 aircraft. *Journal of Atmospheric and Oceanic Technology*, *7*(4), 525–540. https://doi.org/10.1175/1520-0426(1990)007%3C0525:TMMSOT%3E2.0.CO;2

Solomon, S., Rosenlof, K. H., Portmann, R. W., Daniel, J. S., Davis, S. M., Sanford, T. J., & Plattner, G.-K. (2010). Contributions of stratospheric water vapor to decadal changes in the rate of global warming. *Science*, *327*(5970), 1219–1223. https://doi.org/10.1126/science.1182488

Thomas, A., Borrmann, S., Kiemle, C., Cairo, F., Volk, M., Beuermann, J., et al. (2002). In situ measurements of background aerosol and subvisible cirrus in the tropical tropopause region. *Geophysical Research Letters*, *107*(D24), 4763. https://doi.org/10.1029/2001JD001385

Thornberry, T., Rollins, A., Avery, M., Woods, S., Lawson, P., Bui, T., & Gao, R.-S. (2017). Ice water content - extinction relationships and effective diameter for TTL cirrus derived from in situ measurements during ATTREX 2014. *Journal of Geophysical Research: Atmospheres*, *122*, D025948. https://doi.org/10.1002/2016JD025948

Thornberry, T. D., Rollins, A. W., Gao, R. S., Watts, L. A., Ciciora, S. J., McLaughlin, R. J., & Fahey, D. W. (2015). A two-channel, tunable diode laser-based hygrometer for measurement of water vapor and cirrus cloud ice water content in the upper troposphere and lower stratosphere. *Atmospheric Measurement Technology*, *8*(1), 211–224. https://doi.org/10.5194/amt-8-211-2015

Ueyama, R., Jensen, E. J., Pfister, L., & Kim, J.-E. (2015). Dynamical, convective, and microphysical control on wintertime distributions of water vapor and clouds in the tropical tropopause layer. *Journal of Geophysical Research: Atmospheres*, *120*, 10,483–10,500. https://doi.org/10.1002/2015JD023318

Ulanowski, Z., Hesse, E., Kaye, P. H., & Baran, A. J. (2006). Light scattering by complex ice-analogue crystals. *Journal of Quantitative Spectroscopy & Radiative Transfer*, *100*(1-3), 382–392. https://doi.org/10.1016/j.jqsrt.2005.11.052

Wendisch, M., Yang, P., & Pilewskie, P. (2007). Effects of ice crystal habit on thermal infrared radiative properties and forcing of cirrus. *Journal of Geophysical Research*, *112*, D08201. https://doi.org/10.1029/2006JD007899

Westbrook, C. (2008). The fall speeds of sub-100 μm ice crystals. *Quarterly Journal of the Royal Meteorological Society*, *134*(634), 1243–1251. https://doi.org/10.1002/qj.290

Whiteway, J., Cook, C., Gallagher, M., Choularton, T., Harries, J., Connolly, P., et al. (2004). Anatomy of cirrus clouds: Results from the Emerald airborne campaign. *Geophysical Research Letters*, *31*, L24102. https://doi.org/10.1029/2004GL021201

Yang, P., Liou, K. N., Bi, L., Liu, C., Yi, B. Q., & Baum, B. A. (2015). On the radiative properties of ice clouds: Light scattering, remote sensing, and radiation parameterization. *Advances in Atmospheric Sciences*, *32*(1), 32–63. https://doi.org/10.1007/s00376-014-0011-z